

# Numerical study of mass and heat transport in solid-oxide fuel cells running on humidified methane

Vinod M. Janardhanan, Olaf Deutschmann\*

*Institute for Chemical Technology and Polymer Chemistry, University of Karlsruhe, Engesserstr 20, D-76131 Karlsruhe, Germany*

Received 16 June 2006; received in revised form 18 January 2007; accepted 19 January 2007

Available online 4 February 2007

## Abstract

Internally reforming anode supported solid-oxide fuel cells (SOFC) running on humidified CH<sub>4</sub> is studied numerically. The computational framework employs detailed multi-step models for heterogeneous chemistry for Ni catalysts. The electrochemistry is implemented using a modified Butler–Volmer setting based on elementary charge transfer kinetics. Transport through the porous matrix is modeled using the dusty gas model (DGM). Parameters required for the electrochemical model are adjusted to reproduce experimentally observed data. Obtained parameters are then used to model a co-flow planar single cell under internally reforming conditions assuming the interconnect walls as adiabatic. Numerous runs with varying inlet conditions of cathode stream are carried out to deduce the behavior of temperature and current density distribution in the cell. Results show that internal reforming generally leads to a temperature drop near the inlet boundary.

© 2007 Elsevier Ltd. All rights reserved.

*Keywords:* SOFC; Internal reforming; Heat transfer; Heterogeneous chemistry

## 1. Introduction

Solid-oxide fuel cells (SOFCs) offer the possibility of clean energy production by utilizing a variety of fuels. Natural gas is considered as an ideal fuel for stationary SOFC applications due to its wide spread availability and distribution infrastructure. A range of hydrocarbons can be utilized in SOFC with or without upstream fuel processing. In the case of upstream fuel processing an external fuel processor can be used in front of the stack to produce a reformat fuel which is rich in synthesis gas (H<sub>2</sub> and CO). Alternatively the reforming process can be carried out within the cell stack in two different manners: (1) indirect internal reforming and (2) direct internal reforming. In the case of indirect internal reforming the reforming unit can be integrated to the SOFC stack, which further utilizes the heat generated by the cells. In case of direct internal reforming, the reforming process is carried out directly on the anode of the cell which is catalytically active. However, if the operating conditions and anode materials are not chosen carefully

the direct internal reforming of hydrocarbons (HC), especially for higher HC, can lead to coke formation within the anode which can finally lead to the complete failure of the cell (Steele, 1999; Finnerty et al., 1998). Certain recent studies reported the direct electrochemical oxidation of HC using anode materials resistant towards carbon formation (Murray et al., 1999; Park et al., 2000). Others have studied the effect of precious metal dopants on anodes to decrease the coking propensity (McIntosh et al., 2003; Takeguchi et al., 2003) and demonstrated the use of bimetallics in ceria based anodes to reduce coking (Lee et al., 2004). The present work focuses on the interactions of heat transport, mass transport, heterogeneous chemistry, and electrochemistry under internal reforming conditions in a Ni–YSZ anode supported cell using a quasi two-dimensional computational framework.

Modeling the processes in a SOFC is a challenging task due to the coupled interactions of transport, chemistry, and electrochemistry. Understanding the interactions of the above is critical for optimal cell design. There are several studies on the modeling of SOFCs, starting from simple polarization models to stack based models. Each of these studies vary in the assumptions made and in the dimensionality of the problem. Chan et al. have reported studies based on simple analytical

\* Corresponding author. Tel.: +49 721 6083138; fax: +49 721 6084805.  
E-mail address: deutschmann@ict.uni-karlsruhe.de (O. Deutschmann).

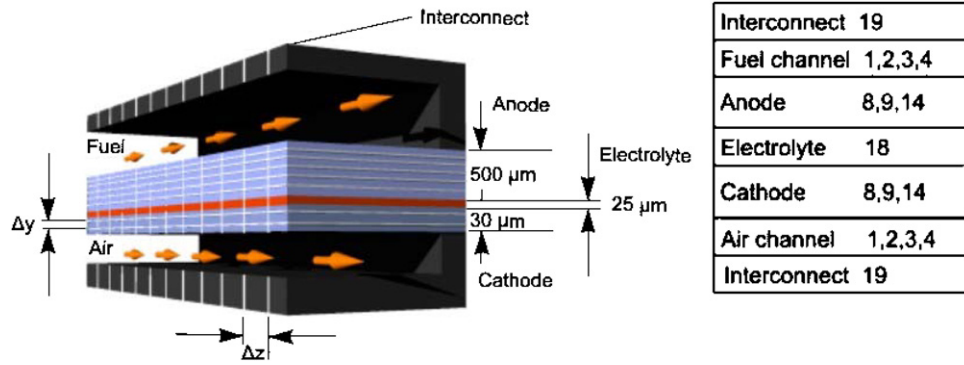


Fig. 1. Finite volume representation of the geometry under consideration and the equation system solved for various components.

Table 1  
SOFC parameters

Parameters	Values	Units
<i>Anode</i>		
Thickness ( $l_a$ )	0.50	mm
Average pore radius ( $r_p$ )	0.50	$\mu\text{m}$
Average particle diameter ( $d_p$ )	2.50	$\mu\text{m}$
Specific area ( $A_s$ )	1025	$\text{cm}^{-1}$
Porosity ( $\phi$ )	0.35	
Tortuosity ( $\tau$ )	3.80	
Charge-transfer coefficient ( $\beta_a$ )	0.50	
<i>Electrolyte</i>		
Thickness ( $l_e$ )	25.0	$\mu\text{m}$
<i>Cathode</i>		
Thickness ( $l_c$ )	30.0	$\mu\text{m}$
Average pore radius ( $r_p$ )	0.50	$\mu\text{m}$
Average particle diameter ( $d_p$ )	2.50	$\mu\text{m}$
Porosity ( $\phi$ )	0.35	
Tortuosity ( $\tau$ )	3.80	
Charge-transfer coefficient ( $\beta_a$ )	0.45	

models (Chan et al., 2001, 2004; Chan and Xia, 2001). Zhu and Kee (2003) reported a general numerical model to describe the polarization effects, which can handle any fuel composition and also the concept of direct use of HCs. In a previous study we reported the isothermal operation of planar SOFC on pre-reformed fuel (Zhu et al., 2005). Keegan et al. (2002) reported a stack level model for a cross flow planar SOFC. Haberman and Young (2004) and Costmagna et al. (2004) studied the operation of integrated planar SOFC. Li et al. (Li et al., 2004; Li and Suzuki, 2004) and Hall (1999) have reported numerical studies on tubular SOFC.

In the present theoretical study we report a mechanism based on heterogeneous the non-isothermal operation of a co-flow planar anode supported SOFC under direct internal reforming conditions. The approach utilizes the potential of on elementary reactions for the steam reforming of methane on Ni catalysts. The following sections encompass the modeling framework adopted in this work. A schematic representation of the model geometry under consideration and the equation system solved for various components are shown in Fig. 1. The unit cell is

assumed to be anode supported with 500  $\mu\text{m}$  anode and 5 cm in length. Other parameters concerning the geometry are given in Table 1.

## 2. Model description

### 2.1. Fluid and energy transport

#### 2.1.1. Channel flow

Flow through fuel and air channels is assumed to be one dimensional and laminar in nature. The plug flow equation for species continuity in the channels is given by

$$\frac{\partial(\rho_f Y_k)}{\partial t} = -\frac{\partial(\rho_f v Y_k)}{\partial z} + \frac{P_e}{A_c} J_k W_k, \quad k = 1, \dots, K_g. \quad (1)$$

The mass balance equation is used as

$$\frac{\partial \dot{m}}{\partial t} = -\frac{\partial(\dot{m}v)}{\partial z} + v \sum_{k=1}^{K_g} \frac{P_e}{A_c} J_k W_k, \quad (2)$$

where  $P_e$  is the perimeter associated with the membrane electrode assembly (MEA) and  $A_c$  is the cross sectional area of the channel. Assuming constant pressure in the channels the density is calculated from the ideal gas equation

$$p\bar{M} = \rho_f RT. \quad (3)$$

In Eqs. (1) and (2)  $J_k$  is the flux at the electrode channel interface and is calculated using the dusty gas model (DGM) (Eq. (10)). Temperatures in the flow channels are determined from the energy equation

$$\begin{aligned} \frac{\partial(\rho_f C_{pf} T_f)}{\partial t} = & -\frac{\partial(v\rho_f C_{pf} T_f)}{\partial z} - \frac{h}{H_c}(T_f - T_e) \\ & + \frac{h}{H_c}(T_I - T_f). \end{aligned} \quad (4)$$

The first term on the right-hand side of Eq. (4) represents the transport of energy due to the bulk fluid flow, the second and third terms represent the heat transfer from the channel to the electrode structure and the heat transferred from the interconnect into the flow channels, respectively. The heat transfer

coefficient  $h$  is evaluated from the Nusselt number

$$Nu = \frac{hD_h}{k}, \quad (5)$$

which is expressed empirically as (Hayes and Kolaczowski, 1997)

$$Nu = 3.095 + 8.933 \left( \frac{1000}{Gz} \right)^{-0.5386} \exp \left( -\frac{6.7275}{Gz} \right), \quad (6)$$

where the Graetz number  $Gz$  is given by

$$Gz = \frac{D_h}{z} Re Pr, \quad (7)$$

where  $D_h$  is the hydraulic diameter,  $z$  the axial position,  $Re$  the Reynolds number, and  $Pr$  is the Prandtl number.

### 2.1.2. Porous media transport

Species transport through the porous media is assumed to be one dimensional across the thickness of the porous structure and is given by

$$\frac{\partial(\phi \rho_f Y_k)}{\partial t} = -\frac{\partial(J_k W_k)}{\partial y} + \dot{s}_k W_k A_s, \quad (8)$$

where  $\dot{s}_k$  is the molar heterogeneous production rate of the chemical species  $k$  and  $A_s$  is the specific catalyst area available for surface reactions. The total density within the porous structure can be calculated from

$$\frac{\partial(\phi \rho_f)}{\partial t} = -\sum_{k=1}^{K_g} \frac{\partial(J_k W_k)}{\partial y} + \sum_{k=1}^{K_g} \dot{s}_k W_k A_s. \quad (9)$$

In the above equations the fluxes  $J_k$  are evaluated using the DGM. According to DGM, the net species molar flux is given by (Zhu et al., 2005)

$$J_k = - \left[ \sum_{l=1}^{K_g} D_{kl}^{\text{DGM}} \nabla[X_l] + \left( \sum_{l=1}^{K_g} \frac{D_{kl}^{\text{DGM}} [X_l]}{D_{l,kn}^e} \right) \frac{B_g}{\mu} \nabla p \right]. \quad (10)$$

The first term on the right-hand side of Eq. (10) represents the diffusive flux and the second term represents the viscous flux. Though the viscous flux driven by the pressure gradient is negligible compared to diffusive flow in the porous anode (Jiang and Virkar, 2003), we retain the term in our calculations.  $D_{kl}^{\text{DGM}}$  are defined as DGM diffusion coefficients given as (Zhu et al., 2005)

$$D_{kl}^{\text{DGM}} = H^{-1}, \quad (11)$$

where the elements of the  $H$  matrix are

$$h_{kl} = \left[ \frac{1}{D_{k,kn}^e} + \sum_{j \neq k} \frac{X_j}{D_{kj}^e} \right] \delta_{kl} + (\delta_{kl} - 1) \frac{X_k}{D_{kl}^e}. \quad (12)$$

A detailed account of the DGM is given elsewhere (Jackson, 1977; Mason and Malinauskas, 1983). The permeability  $B_g$  in

Eq. (10) is given by Kozeny–Carman relationship (Bear, 1972)

$$B_g = \frac{\phi^3 d_p}{72\tau(1-\phi)^2}. \quad (13)$$

Assuming the reaction heat is released on the solid surface the heat balance equation within the porous structure can be written as

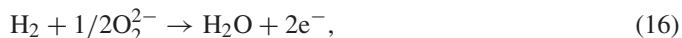
$$\frac{\partial(\rho C_p T)}{\partial t} = \nabla \cdot (k_{\text{eff}} \nabla T) + \frac{h}{\delta y} (T_f - T) - \sum_{k=1}^{K_g} \dot{s} W_k A_s h_k + Q_r + Q_e, \quad (14)$$

where  $C_p$  is the specific heat capacity of the solid material. The first term on the right-hand side represents heat transfer due to conduction and the second term the heat transfer from the channel to the electrodes at the interface. The heat transfer due to gas diffusion is not accounted in the above equation, since it is not significant compared to the conduction in porous media.  $\delta y$  appearing in the second term results from the finite volume integration over the discretized cells and must have a finite value. The fourth and fifth term on the right-hand side of equation Eq. (14) represents the radiative heat transfer between the electrode and the interconnect structure and the heat release due to electrochemical reactions, respectively. The radiation heat source is given by

$$Q_r = \frac{1}{\delta y} \left[ \frac{\sigma(T_I^4 - T^4)}{1/\varepsilon_I + 1/\varepsilon - 1} \right]. \quad (15)$$

### 2.1.3. Electrolyte

The global charge transfer reaction at the three-phase interface can be written as



however, only a part of the energy change during the reaction is released as heat, which amounts to

$$Q_e = -T \Delta S \frac{i}{2F}. \quad (17)$$

Assuming the electrolyte to be one dimensional the heat balance equation reduces to

$$\frac{\partial(\rho C_p T)}{\partial t} = \frac{\partial}{\partial z} \left( k \frac{\partial T}{\partial z} \right) + \frac{i^2}{\sigma_e}. \quad (18)$$

The last term in the above equation represents the ohmic heating due to ion transport in the electrolyte.

### 2.1.4. Interconnect

The heat balance equation for the interconnect can be summarized as

$$\frac{\partial(\rho C_p T_I)}{\partial t} = \frac{\partial}{\partial z} \left( k \frac{\partial T_I}{\partial z} \right) + \frac{h}{H_I} (T_f - T_I) - \frac{1}{H_I} \left[ \frac{\sigma(T_I^4 - T^4)}{1/\varepsilon_I + 1/\varepsilon - 1} \right]. \quad (19)$$

The first term on the right-hand side represents the conduction within the interconnect, the second and third terms represent the heat transferred to/from the channel to the interconnect and the radiation heat transfer to/from the interconnect to the electrode structure. Eqs. (14), (18), and (19) require boundary conditions at  $z = 0$  and  $L$  which are given by

$$\left. \frac{\partial T}{\partial z} \right|_{z=0} = 0, \quad \left. \frac{\partial T}{\partial z} \right|_{z=L} = 0. \quad (20)$$

Modeling radiative heat transfer in a SOFC is a complex process, and the radiative transport within the semitransparent electrodes and electrolyte, and surface to surface heat transfer must be accounted for an accurate calculation. However, an exact knowledge of phenomenological properties like absorption coefficient, refractive index, scattering coefficient, emissivity, reflectivity, etc. are obstacles to model radiative heat transport in SOFC electrodes and electrolyte. Detailed discussions of heat transfer by radiation in SOFCs are given elsewhere (Damm and Federov, 2005a,b; Murthy and Federov, 2003; VanderSteen and Pharoah, 2006). In an analysis of spectral radiation in SOFC electrodes Damm and Federov (2005b) have proven that the radiation effects in SOFC electrodes are minimal and can safely be neglected. Therefore, in the present work, only surface to surface radiation is considered. Since the planar geometry considered here is of high aspect ratio ( $L/d \approx 50$ ) the surfaces can be treated as black bodies with emissivity 1 (Damm and Federov, 2005a).

## 2.2. Heterogeneous chemistry

SOFCs can run on HC fuels without external reforming since the high temperature of operation allows the endothermic reforming reactions (steam reforming and dry reforming, where the rate of steam reforming is higher than that of dry reforming) to produce  $H_2$  and CO. These electrochemically active species further participates in charge transfer chemistry producing  $H_2O$  and  $CO_2$ . The CO produced can also participate in water–gas shift or Boudouard reaction depending on the stoichiometric availability of  $H_2O$  (Clarke et al., 1997). The products of charge transfer chemistry further replenishes reforming chemistry within the cell. Internal reforming eliminates the need of an external reformer and the high air flow rate required for cell cooling, resulting in reduced capital cost and increased overall efficiency of the system. Reforming kinetics of  $CH_4$  on Ni catalysts are well studied and is given elsewhere (Dicks et al., 2000; Xu and Froment, 1989). There are also reports on the catalytic activity of YSZ (Zhu et al., 2004) which is the most commonly used ionic conductor in SOFC components.

Though the reforming reactions are endothermic in nature, the cell reactions and the various losses within the cell are exothermic. It is generally agreed that the cell reactions produce enough heat that can be utilized for carrying out the reforming reactions internally. Under typical operating conditions the heat requirement for steam reforming is half the heat generated in the cell stack (Ahmed and Foger, 2000). Utilizing the cell generated heat for endothermic reforming reactions is an issue which

is considered in detail in the results and discussion of this paper.

In the present study we use a multi-step heterogeneous reaction mechanism, which is evaluated for Ni–YSZ anode supports and in steam assisted catalytic partial oxidation of  $CH_4$  in small channel monolithic reactors using Ni supported on alumina (Hecht et al., 2005). The reaction mechanism consists of 42 reactions among six gas-phase species and 12 surface adsorbed species. More discussions about the mechanism are given elsewhere (Zhu et al., 2005; Hecht et al., 2005). However, in this study we use a modified version of the mechanism which is thermodynamically consistent for a wider temperature range (Janardhanan and Deutschmann, 2006). This modified mechanism is also validated using the experiments reported by Hecht et al. (2005). The limitations of the new mechanism are discussed in Janardhanan and Deutschmann (2006). Comparison against equilibrium predictions shows that the mechanism needs further improvements concerning surface carbon deposition at higher temperatures. However, the gas-phase compositions were in good agreement. Since in this work the feedstock is assumed to be  $CH_4$ , and  $CH_4$  being the most stable HC, any possibility of gas-phase reactions can safely be neglected. However, for the case of higher HCs, significant gas-phase reactions can happen in the fuel channel (Sheng and Dean, 2004).

## 2.3. Electrochemistry

It is well known that  $H_2$  and CO can participate in charge transfer chemistry. However, the rate at which CO is converted in water–gas shift by far exceeds the rate of electrochemical oxidation of CO (Matsusaki and Yasuda, 2000). When both species are present in the system  $H_2$  dominates over CO in the charge transfer chemistry and CO seems to play a minor role and can safely be neglected (Sukeshini et al., 2006). Hence, in the present study we assume that  $H_2$  is the only electrochemically active species. The charge transfer reactions occur at the interface formed by the electrocatalyst, electrolyte and gas-phase boundaries, known as three-phase boundaries (Tanner et al., 1997). In the case of composite electrodes, this reaction zone can spread out into the electrode usually of the order of few  $\sim 10 \mu m$  (Kim et al., 1999; Williford et al., 2003). This is a small fraction of the total thickness of the anode in case of an anode supported cell and hence we can assume the charge transfer reaction to be happening at a limited region near the electrode–electrolyte interface. Therefore in our study we do not consider distributed charge transfer, but only the charge transfer at the electrode–electrolyte interface.

The irreversibility associated with the cell processes leads to various overpotential losses such as activation, ohmic, and concentration losses. A detailed account of the various loss terms is given in Larminie and Dicks (2003). The operating cell voltage is related to various losses as

$$E_{\text{cell}} = E_{\text{rev}} - \eta_a(i) - |\eta_c(i)| - \eta_{\text{ohm}}(i) - \eta_{\text{conc}}(i), \quad (21)$$

where  $\eta_a$  and  $\eta_c$  are the activation losses at the anode and cathode side, respectively,  $\eta_{\text{ohm}}$  is the ohmic overpotential, and

$\eta_{\text{conc}}$  is the concentration overpotential. Since in this work we are modeling porous media transport the concentration overpotential is not treated explicitly.  $E_{\text{rev}}$  is given by the well known Nernst equation

$$E_{\text{rev}} = E^0 + \frac{RT}{2F} \ln \left( \frac{p_{\text{H}_2,a} p_{\text{O}_2,c}^{1/2}}{p_{\text{H}_2\text{O},a}} \right). \quad (22)$$

In the above equation  $E^0$  is the electromotive force (EMF) at standard pressure. The reversible potential is calculated based on the partial pressures of  $\text{H}_2$ ,  $\text{O}_2$ , and  $\text{H}_2\text{O}$  at the three-phase interface. The ohmic loss in Eq. (21) is defined as

$$\eta_{\text{ohm}} = R_{\text{tot}} i, \quad (23)$$

where  $R_{\text{tot}}$  is the total area specific resistance. In modern cells, however, the resistance caused by the anode and cathode materials is negligible compared with the electrolyte resistance. Therefore in the following analysis only the resistance contributed by the electrolyte, i.e.,  $R_e$  is considered, which is defined as

$$R_e = \frac{l_e}{\sigma_e}, \quad (24)$$

where  $l_e$  is the thickness of the electrolyte, and  $\sigma_e$  is the electrolyte conductivity defined as a function of temperature

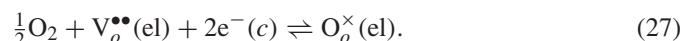
$$\sigma_e = 3.34 \times 10^4 \exp \left( -\frac{10300}{T} \right). \quad (25)$$

The above equation is valid for YSZ electrolyte material and gives an ionic conductivity of  $2.26 \text{ S m}^{-1}$  at 1073 K and  $0.086 \text{ S m}^{-1}$  at 1273 K, which is consistent with the reported values in Larminie and Dicks (2003).

The functional relation between the activation losses and current density is described by a modified Butler–Volmer formalism. For hydrogen oxidation this takes the form

$$i = i_0 \left[ \exp \left( \frac{(1 + \beta_a) F \eta_a}{RT} \right) - \exp \left( -\frac{\beta_c F \eta_a}{RT} \right) \right]. \quad (26)$$

The overall oxygen reduction reaction and the incorporation of the ions into the electrolyte can be written in Kröger–Vink notation as



The above global reaction can be split into a number of steps. One of the possible sequence of mechanistic steps is described below.

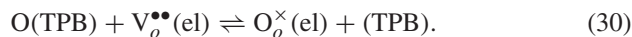
(1) Adsorption/desorption of oxygen



(2) Surface diffusion to three-phase boundary (TPB) regions



(3) Formation of  $\text{O}^{2-}$  ions and the subsequent incorporation into the electrolyte



Assuming the charge transfer step 30 to be rate limiting, Zhu et al. (2005) derived the expressions for Butler–Volmer equation

$$i = i_0 \left[ \exp \left( \frac{\beta_a F \eta_c}{RT} \right) - \exp \left( -\frac{\beta_c F \eta_c}{RT} \right) \right], \quad (31)$$

where  $i_0$  is the exchange current density and  $\beta$  is the asymmetry factor. In general, the activation overpotential  $\eta_c$  on the cathode side is larger compared to the anode side  $\eta_a$ .

In the present study the exchange current density is expressed as a function of temperature and the partial pressures of the reactants and products participating in the charge transfer chemistry. For hydrogen oxidation the exchange current density is given as

$$i_0 = i_{\text{H}_2}^* \frac{(p_{\text{H}_2}/p_{\text{H}_2}^*)^{1/4} (p_{\text{H}_2\text{O}})^{3/4}}{1 + (p_{\text{H}_2}/p_{\text{H}_2}^*)^{1/2}}, \quad (32)$$

and for oxygen reduction

$$i_0 = i_{\text{O}_2}^* \frac{(p_{\text{O}_2}/p_{\text{O}_2}^*)^{1/4}}{1 + (p_{\text{O}_2}/p_{\text{O}_2}^*)^{1/2}}. \quad (33)$$

Here  $i_i^*$  is an adjustable parameter and is expressed as a function of temperature

$$i_i^* = k_i \exp \left( -\frac{E_i}{RT} \right). \quad (34)$$

Expressions for  $p_{\text{H}_2}^*$  and  $p_{\text{O}_2}^*$  can be found in Zhu et al. (2005).

#### 2.4. Solution procedure

Eqs. (1)–(4), (8), (9), (14), (18), and (19) form a system of coupled non-linear equations, which can be written in the residual form as

$$F(\Phi) = 0, \quad (35)$$

where the vector  $\Phi$  is given by

$$\Phi = [(T)_{\text{ic}}, (Y, \dot{m}, T)_a, (Y, \rho, T, \theta)_{a,1} \dots (Y, \rho, T, \theta)_{a,n}, (T)_e, (Y, \rho, T)_{c,1}, \dots (Y, \rho, T)_{c,m}, (Y, \dot{m}, T)_c, (T)_{\text{ic}}]^T. \quad (36)$$

To solve the equation system they are first cast into a finite volume form. The channels, interconnects, and electrolyte are treated as one dimensional and the reactor geometry is discretized in the axial direction into 200 cells. The anode is discretized into 25 cells along the thickness and the cathode into 10 cells. The finite volume discretization allows to define the variables at the cell centers or at cell faces. In our scheme the fluxes are defined at the cell faces, while all other properties

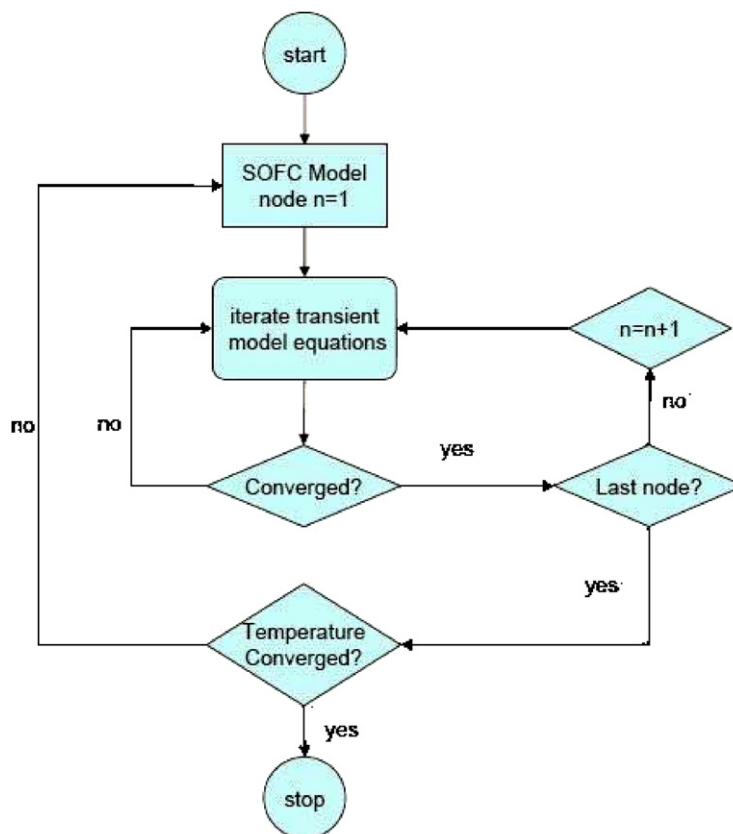


Fig. 2. Flowchart of solution algorithm for the equation systems.

are defined at the cell centers. In calculating the diffusive flux  $J_k$  at the channel–electrode interface the concentrations at the interface are assumed to be the same as those in the bulk of the gas. The entire solution procedure follows a space marching algorithm: at each axial position the transient system of equations are solved until a steady state solution is obtained. The initial condition at each axial position assumes the converged solution from the previous finite volume cell. Due to the elliptic nature of the heat balance equation in porous electrodes and the conductive terms in the solid regions an outer iteration loop is formed around the marching algorithm. The equation system is solved using the differential algebraic equation (DAE) solver LIMEX (Deuffhardt et al., 1987). The entire solution procedure converges in few passes. A flow chart for the solution process is shown in Fig. 2.

The solution of the porous media problem also requires the current density at the TPB. The current density is calculated from the system of algebraic electrochemical model equations (21), (26), and (31). The unknowns can be written in the vector form as

$$\Phi = [i, \eta_a, \eta_c]^T. \quad (37)$$

This equation system is solved using a damped Newton iteration, which converges in three to four integrations.

The software is written in FORTRAN 77 and integrated into the detailed chemistry software package DETCHEM (Deutschmann et al., 2004).

In the solution procedure adopted here, the button cell experiments reported by Liu and Barnett (2003) are simulated to obtain realistic electrochemical model parameters. The parameters thus obtained are further used for a planar unit cell simulation. In this way we ensure that the model parameters used for single cell simulation are in concert with experimental data.

## 2.5. Results and discussion

In the examples discussed here we focus our attention on the performance of humidified ( $\sim 3\% \text{H}_2\text{O}$ ) methane entering a planar SOFC at  $800^\circ\text{C}$  and  $0.3 \text{ m s}^{-1}$ . For the base case considered here, air is assumed to enter the cathode channel at  $1.5 \text{ m s}^{-1}$  and  $650^\circ\text{C}$ . Button cell simulations are carried out to reproduce the experimental data reported by Liu and Barnett (2003) and hence to deduce the electrochemical model parameters. The authors report high power densities for direct operation on methane. The MEA structure consists of  $0.5 \text{ mm}$  Ni–YSZ anode with  $25 \mu\text{m}$  YSZ electrolyte and  $30 \mu\text{m}$  LSM cathode. Table 1 lists the parameters used to represent the MEA. The exchange current parameters used to fit the experimental data are given in Table 3. A detailed description of these button cell simulations is reported in Janardhanan and Deutschmann (2006). In brief the only parameters adjusted to reproduce the experimental observations are the activation energy and pre-exponential factors in Eq. (34). The activation energies are found to be in

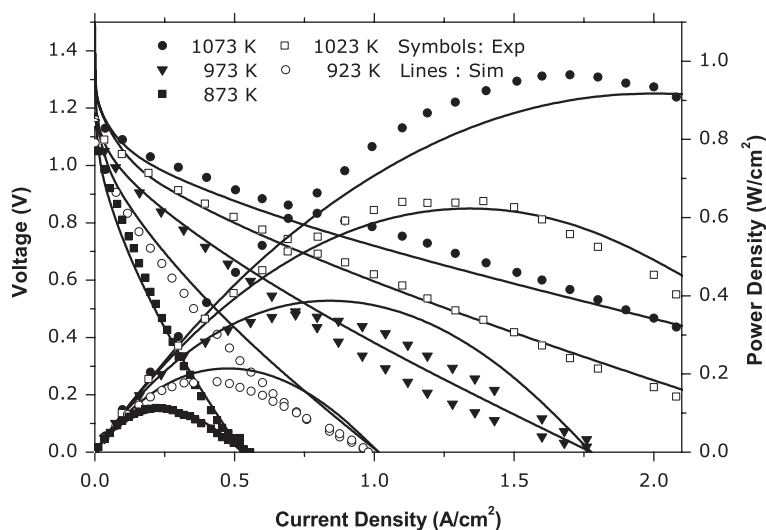


Fig. 3. Voltage and power density against current density. Comparison with experimental data (Liu and Barnett, 2003).

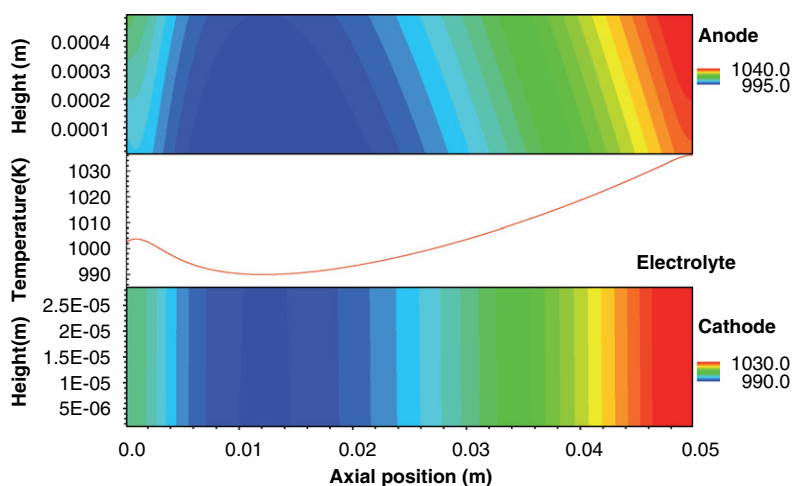


Fig. 4. Temperature profile within the membrane electrode assembly, top panel shows the anode, middle one the electrolyte and the bottom panel shows the cathode.

good agreement with the experiments on Ni patterned anodes (Bieberle, 2000). Comparison of simulated and reported experimental data is given in Fig. 3. The model parameters reasonably reproduce the experimental observation. However, at the highest temperature of 800 °C the maximum power density is under predicted. In general the current–voltage curves are linear at high current densities. However, concavity of the curve increases with decreasing temperature indicating the dominance of activation losses. Even at high temperature in the realm of low current density activation losses are dominant. The agreement between the experimental observation and simulation data supports the assumption of H<sub>2</sub> as the electrochemically active species even for the case of HC rich feed.

Assuming the outer walls of the interconnects to be adiabatic, Figs. 4–6 illustrate the temperature profiles within the various components of the unit cell under consideration. Material properties used for the simulations are given in Table 2. Parameters for exchange current density, five in Table 3, are taken from

Janardhanan and Deutschmann (2006). Fig. 4 shows the temperature profiles within the MEA. The top panel of the figure shows the temperature profile within the anode, the middle one the electrolyte and the bottom one the cathode. Within the MEA structure the resulting temperature profile is the net effect of heat absorbed or released as a result of heterogeneous chemical reactions, heat release due to the electrochemical reaction at the TPB, resistive heating within the electrolyte, convective heat transfer to and from the channels, and the radiative heat transfer with the interconnects. Near the inlet section, the temperature drops as a result of endothermic reforming reaction. However, further downstream the unit cell the temperature start to increase as a result of exothermic cell reactions. It is evident from Fig. 6 that the fuel stream loses heat to the comparatively cold air entering the air channel. As a result the temperature of the air stream increases from 650 °C to approximately 680 °C near the inlet (Fig. 5). However, as reforming starts the air channel temperature starts to drop. Both air and fuel channel temperature

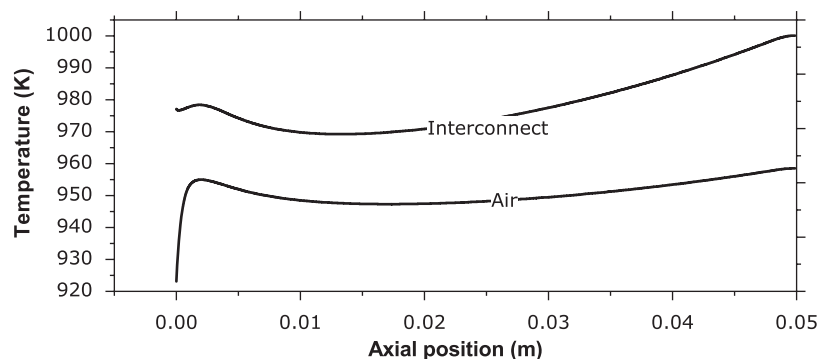


Fig. 5. Temperature profile within the air channel and cathode side interconnect along the length of unit cell.

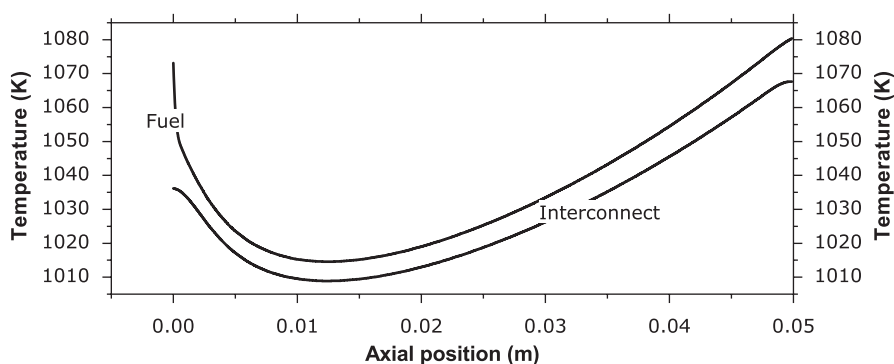


Fig. 6. Temperature profiles within the fuel channel and the anode side interconnect along the length of the unit cell.

Table 2  
Material properties

Parameters	Values	Units
<i>Interconnect</i>		
Thickness ( $l_i$ )	300	$\mu\text{m}$
Specific heat ( $C_p$ )	550.0	$\text{J kg}^{-1} \text{K}^{-1}$
Thermal conductivity ( $k$ )	20.0	$\text{J m}^{-1} \text{s}^{-1} \text{K}^{-1}$
Density ( $\rho$ )	3030.0	$\text{kg m}^{-3}$
<i>Electrolyte</i>		
Specific heat ( $C_p$ )	470.0	$\text{J kg}^{-1} \text{K}^{-1}$
Thermal conductivity ( $k$ )	2.16	$\text{J m}^{-1} \text{s}^{-1} \text{K}^{-1}$
Density ( $\rho$ )	5160.0	$\text{kg m}^{-3}$
<i>Cathode</i>		
Specific heat ( $C_p$ )	430.0	$\text{J kg}^{-1} \text{K}^{-1}$
Thermal conductivity ( $k$ )	5.84	$\text{J m}^{-1} \text{s}^{-1} \text{K}^{-1}$
Density ( $\rho$ )	3030.0	$\text{kg m}^{-3}$
<i>Anode</i>		
Specific heat ( $C_p$ )	450.0	$\text{J kg}^{-1} \text{K}^{-1}$
Thermal conductivity ( $k$ )	1.86	$\text{J m}^{-1} \text{s}^{-1} \text{K}^{-1}$
Density ( $\rho$ )	3310.0	$\text{kg m}^{-3}$

Table 3  
Parameters for exchange current density

Parameters	Value	Units
<i>H<sub>2</sub> oxidation (<math>i_{\text{H}_2}^*</math>)</i>		
$k_{\text{H}_2}$ ( $\text{A cm}^{-2}$ )	$207 \times 10^3$	$\text{A cm}^{-2}$
$E_{\text{H}_2}$ ( $\text{kJ mol}^{-1}$ )	87.8	$\text{kJ mol}^{-1}$
<i>O<sub>2</sub> reduction (<math>i_{\text{O}_2}^*</math>)</i>		
$k_{\text{O}_2}$ ( $\text{A cm}^{-2}$ )	$51.9 \times 10^3$	$\text{A cm}^{-2}$
$E_{\text{O}_2}$ ( $\text{kJ mol}^{-1}$ )	88.6	$\text{kJ mol}^{-1}$

is a significant temperature difference between the air stream and the cathode side interconnect. The electrolyte temperature begins to increase near the inlet mainly due to the heat gained from the anode side fuel as well as the resistive heating within the electrolyte. It should be noted that in reality within a cell stack the temperature boundary condition for a unit cell is governed by the surrounding cell temperatures. Furthermore each unit cell's temperature also depends on its position within the stack. However, an analysis like the one carried out here helps to understand the possible temperature distribution and hence the thermal miss-matches within a unit cell as a result of direct internal reforming of any hydrocarbon stream.

Fig. 7 shows the current density and the reversible potential for the unit cell operating at a cell potential of 0.7 V. As expected the reversible potential peaks near the channel inlet and drops further down the length. The initial increase in reversible potential results from the drop in temperature as a result of

start to increase further down the channel length due to the heat liberated within the MEA structure. Both Figs. 5 and 6 show the temperature of the interconnect structures. There is no significant difference in temperature between the anode side interconnect and the fuel channel temperature. However, there

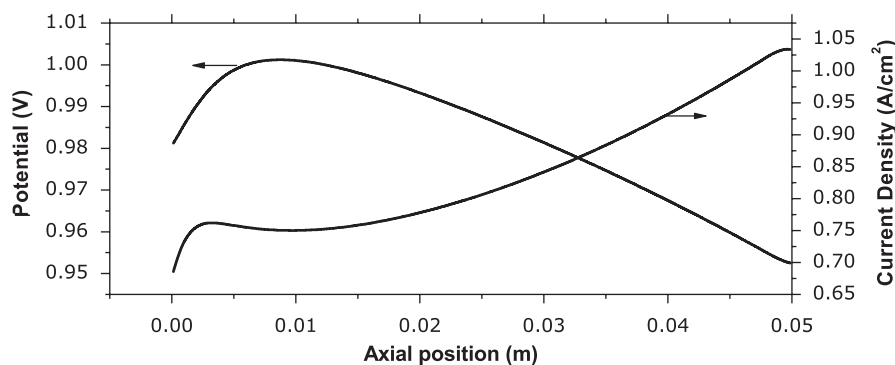


Fig. 7. Current density and reversible potential as a function of reactor length with  $E_{\text{cell}} = 0.7 \text{ V}$ .

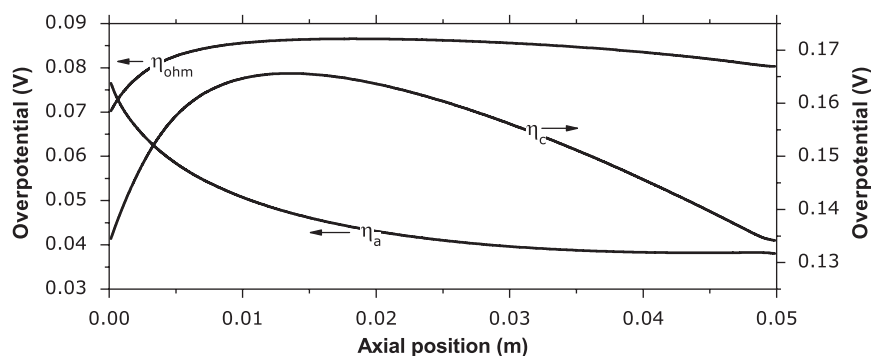


Fig. 8. Over potential losses as a function of reactor length.

reforming reactions. An increase of open circuit potential with decreasing temperature is typical for hydrogen oxidation mechanism, which is the basic assumption for the electrochemical model adopted here. However, down the unit cell length the reversible potential drops due to the increase in temperature as well as the increased fuel dilution due to the production of  $\text{H}_2\text{O}$  at the TPB. The current density begins to increase near the inlet, however, starts to decrease as temperature drops and as the temperature increases the current density also increases. As long as enough fuel is present in the system which can be electrochemically oxidized (in this case  $\text{H}_2$ ), the current density depends strongly on the temperature than on the fuel dilution effect. Fuel dilution at constant temperature would definitely bring down the current density. However, for the case considered here, down the length of the unit cell the temperature increases continuously and the fuel composition becomes more and more rich in  $\text{H}_2$  which is assumed to be the electrochemically active species (Fig. 9). Fig. 8 shows various losses as a function of position along the unit cell. As expected the cathode side losses by far exceed the anode side losses, which is quite typical for SOFCs.

The variations in the species composition in the fuel channel as a result of chemical and electrochemical reactions in the MEA are illustrated in Fig. 9. All reaction products increase down the channel.  $\text{CH}_4$  undergoes heterogeneous reforming within the anode producing  $\text{H}_2$ . The  $\text{H}_2$  so produced further participates in the charge transfer chemistry at the three-phase interfaces producing more  $\text{H}_2\text{O}$ . It should be noticed that  $\text{H}_2\text{O}$

is solely a result of electrochemical reactions. The electrochemically produced  $\text{H}_2\text{O}$  can further participate in reforming to produce synthesis gas as well as in water–gas shift reactions. The  $\text{CO}_2$  produced from the water–gas shift can also participate in reforming and hence contribute to produce more  $\text{H}_2$ . It should be noticed that the off gas of the cell is still a  $\text{CH}_4$  rich fuel.  $\text{CH}_4$  conversion for the case presented here is 51.3%. The fuel utilization can further be increased by increasing the residence time.

Figs. 10–12 show the species profiles and the surface coverages within the anode at three different positions along the unit cell length. Fig. 10 shows the conditions near the inlet, Fig. 11 that at the middle of the cell, and Fig. 12 at the cell exit. In all cases  $\text{H}_2$  and  $\text{H}_2\text{O}$  show opposite fluxes, with the flux of  $\text{H}_2$  towards the TPB where it is consumed electrochemically and  $\text{H}_2\text{O}$  away from the TPB where it is produced. Similarly  $\text{CH}_4$  also has a flux into the anode where it undergoes steam reforming or dry reforming with  $\text{CO}_2$ . It is quite interesting to notice that the profiles are very much non-linear near the channel inlet, while showing linear behavior in other cases. All the three figures also show the surface converges of various adsorbed species. In all cases,  $\text{CO}$  and  $\text{H}_2$  were found to be the major species covering the surface. Near the channel inlet  $\text{Ni}$  remains relatively open in the vicinity of anode channel interface and more  $\text{CO}$  starts to cover the surface near the TPB. From the middle section onwards the surface coverages of hydrogen and  $\text{CO}$  remain nearly constant, but covering more surface than that was found near the inlet section.

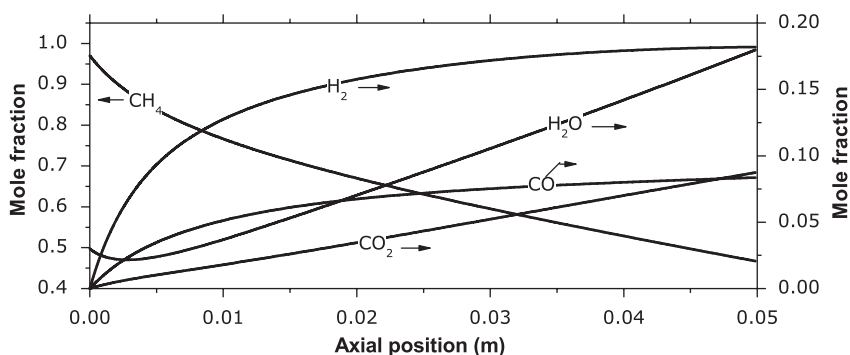


Fig. 9. Mole fraction of various species in the fuel channel along the length of the reactor.

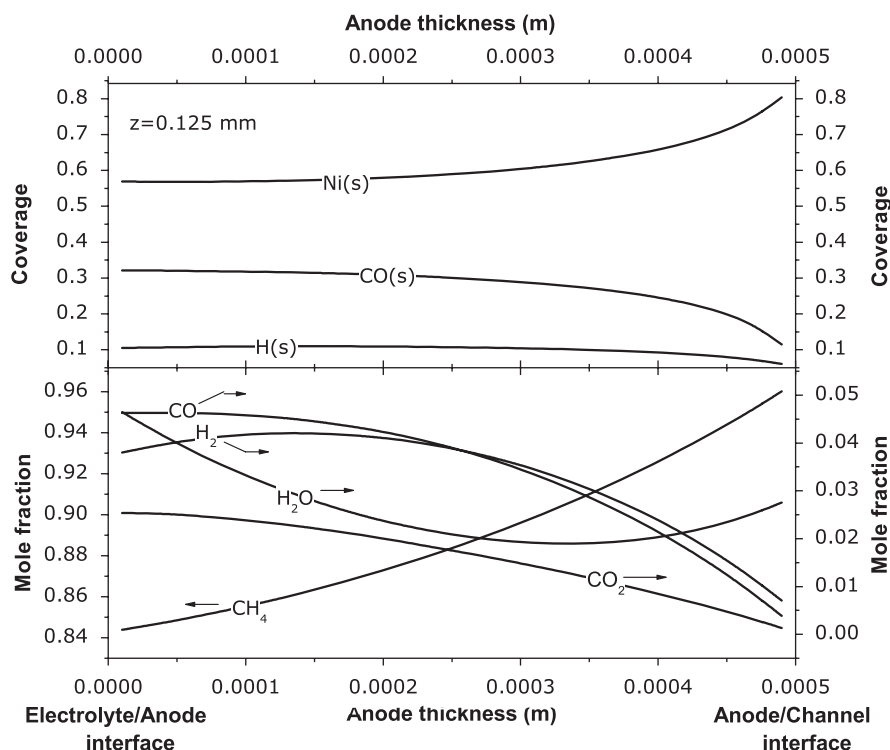


Fig. 10. Species profiles and surface coverages within the anode near the inlet section ( $z = 0.125$  mm). Top panel shows the surface coverage and bottom panel shows species profiles.

Understanding the processes near the TPB would be the key to further improvement of SOFC performance. The surface coverages of various reaction intermediates near the TPB can play a significant role in determining the rate limiting step. Fig. 13 shows the surface coverages of hydrogen, CO and the uncovered Ni surfaces along the TPB. CO is found to be the species covering the major part of the surface, with the coverage increasing from the inlet section and slightly falling off near the exit. Surface coverage of hydrogen is plotted against the Y1 axis. As observed in the gas-phase hydrogen coverage increases from the inlet towards the exit. Though the oxygen coverages is very small it is nevertheless found to be present the TPB and is plotted against Y2 axis. It should be noticed that oxygen on the surface mainly results from the dissociative adsorption of H<sub>2</sub>O. Oxygen coverage decreases initially and increase again

as more and more H<sub>2</sub>O is produced. The presence of reaction intermediates in the immediate vicinity of the TPB can reduce the availability of free surface for H<sub>2</sub> adsorption and the subsequent electrochemical oxidation. Surface diffusion of the adsorbed species can also play a role in deciding the rate limiting step, at least in the high current region (Williford et al., 2003). It is quite evident from Fig. 13 that open sites (Ni(s)) are maximum in the region of low current (near the inlet) where the demand for TPB is low. Though the mechanism is not thoroughly validated for the case of carbon formation, Fig. 14 shows qualitative information regarding the carbon deposition within the cell along the TPB. As observed in experiments a higher current density is found to mitigate coke formation. Fig. 15 shows the profile of oxygen along the channel. Near the inlet the rate of O<sub>2</sub> consumption is found to have a maximum due to the

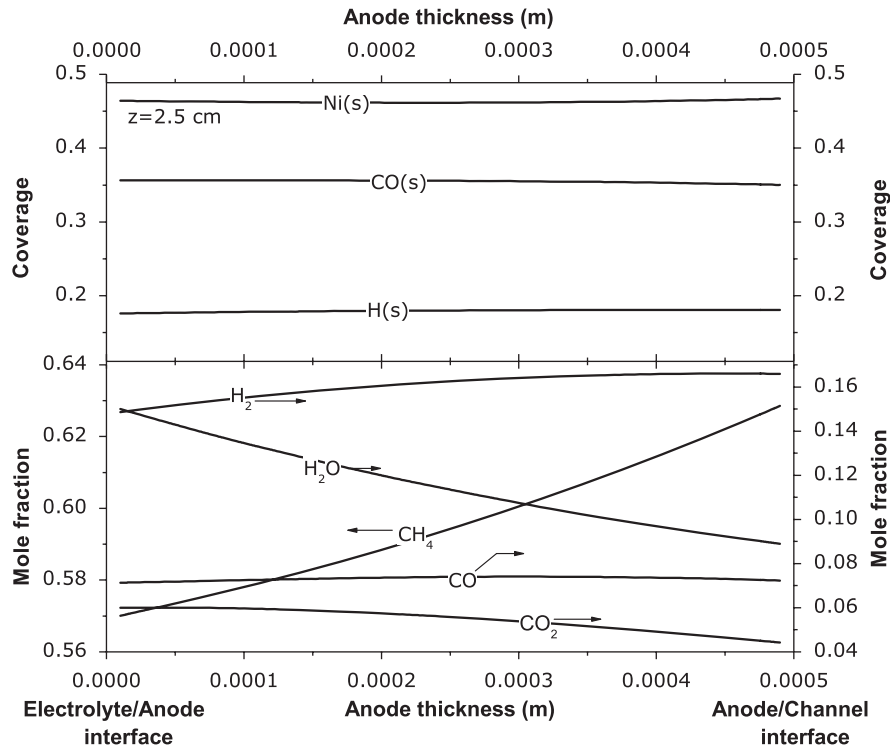


Fig. 11. Species profiles and surface coverages within the anode at half way from the inlet ( $z = 2.5125$  cm). Top panel shows the surface coverage and bottom panel shows species profiles.

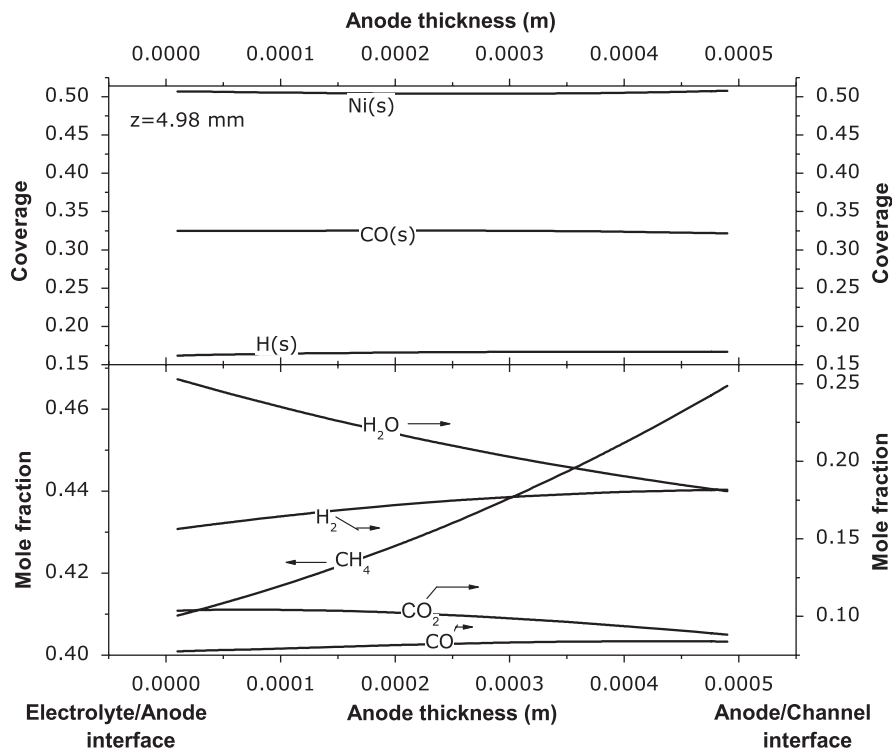


Fig. 12. Species profiles and surface coverages within the anode near the reactor exit ( $z = 4.9875$  mm). Top panel shows the surface coverage and bottom panel shows species profiles.

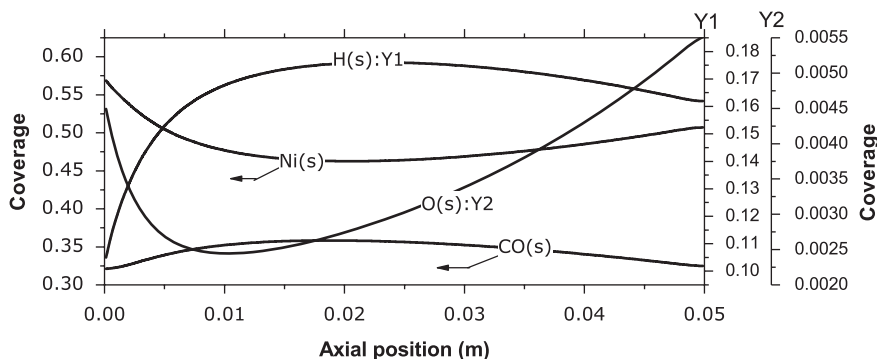


Fig. 13. Surface coverages of the major surface adsorbed species at the three-phase boundary along the length.

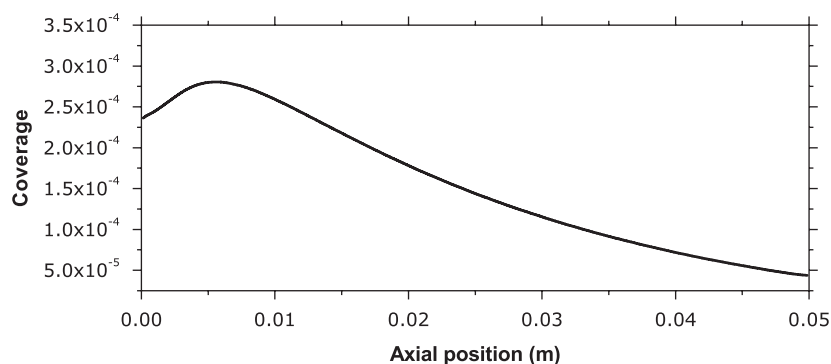


Fig. 14. Surface coverages of carbon along the three-phase boundary.

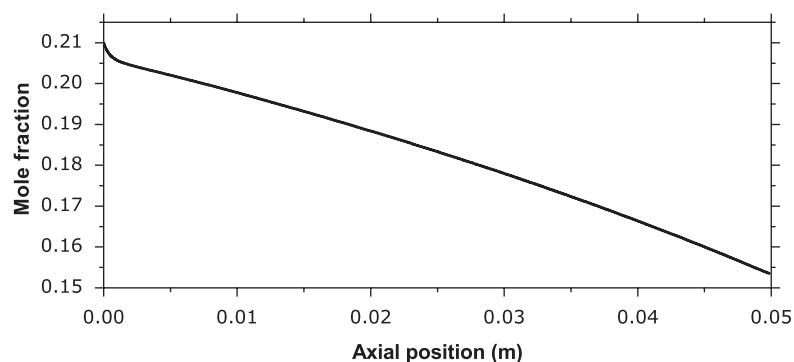


Fig. 15. Mole fraction of oxygen in the air channel along the length of the reactor.

increase in current density. For the case considered here  $O_2$  utilization is 26%.

To understand the behavior of temperature and current density distribution on air inlet conditions, simulations are carried out with the following conditions. (a) at  $650^\circ\text{C}$  and  $3\text{ m s}^{-1}$  (b)  $800^\circ\text{C}$  and  $1.5\text{ m s}^{-1}$ . In all cases the current density, temperature and species profiles were found to follow the same pattern. A higher air inlet temperature was found to result in higher current density. Various values for the base case and cases (a) and (b) are given in Table 4. The table lists the average value of current density, reversible potential, activation and ohmic losses,  $\text{CH}_4$  conversion and  $O_2$  utilization, and the exit temperatures of the fuel and air channel, respectively.

## 2.6. Conclusions

We have studied the operation of a planar SOFC using a  $\text{CH}_4$  rich fuel under internal reforming conditions. The electrochemical parameters used in the model well reproduce the experimental data. It was found that the direct internal reforming can lead to a drop in cell temperature near the inlet and, hence utilizing the cell-produced heat for reforming reaction is not possible in the case of co-flow configuration because the cell generates heat further down the channel. A counter flow configuration would be more appropriate for utilizing the cell generated heat for the endothermic reforming reactions, which will be described in a forthcoming paper. Effects of air inlet

Table 4  
Effect of air inlet conditions on electrochemical model parameters and other fuel and air channel variables

Case	$i$ ( $\text{A cm}^{-2}$ )	$E_{\text{rev}}$ (V)	$\eta_a$ (V)	$\eta_c$ (V)	$\eta_{\text{ohm}}$ (V)	$\text{CH}_4$ (%)	$\text{O}_2$ (%)	$T_f$ (K)	$T_{\text{air}}$ (K)
Base	0.8387	0.9831	0.0448	0.1541	0.0827	55.19	26.3	1080.3	958.5
(a)	0.7815	0.9896	0.0438	0.1626	0.0832	53.9	12.5	1074.2	942.8
(b)	1.2024	0.9527	0.0521	0.1243	0.0762	66.5	40.5	1145.3	1074.2

conditions have been studied by keeping the fuel inlet conditions constant. It was found that a higher air inlet can result in higher current density and higher waste heat production. A qualitative study of coke formation shows that in the case of internal reforming coking can occur near the reactor inlet. The fuel composition considered here resulted in a hydrogen rich off gas for a 5 cm long channel. Anode gas recirculation would be an attractive option in such cases or even a longer fuel cell reactor would be much more efficient from the point of view of fuel utilization.

## Notation

$A_c$	area of cross section, $\text{m}^2$
$A_s$	specific area, $\text{m}^{-1}$
$C_p$	specific heat, $\text{J kg}^{-1} \text{K}^{-1}$
$D_{kl}^e$	effective binary diffusion, $\text{m}^2 \text{s}^{-1}$
$D_{l,kn}^e$	effective Knudsen diffusion, $\text{m}^2 \text{s}^{-1}$
$D_h$	hydraulic diameter, m
$E$	activation energy, $\text{J mol}^{-1}$
$E_{\text{cell}}$	operating cell potential, V
$E_{\text{rev}}$	Nernst potential, V
$F$	Faraday's number, $\text{A mol}^{-1}$
$Gz$	Graetz number
$h$	heat transfer coefficient, $\text{J m}^2 \text{s}^{-1} \text{K}^{-1}$
$H_c$	channel height, m
$i$	current density, $\text{A cm}^{-2}$
$i_0$	exchange current density, $\text{A cm}^{-2}$
$J_k$	species fluxes, $\text{mol m}^{-2} \text{s}^{-1}$
$k$	thermal conductivity, $\text{J m}^{-1} \text{s}^{-1} \text{K}^{-1}$
$K$	number of gas-phase species
$\dot{m}$	mass flux, $\text{Kg m}^{-2} \text{s}^{-1}$
$\bar{M}$	average Molecular mass, $\text{Kg mol}^{-1}$
$Nu$	Nusselt number
$p$	pressure, Pa
$P_e$	perimeter, m
$Pr$	Prandtl number
$R$	gas constant, $\text{J mol}^{-1} \text{K}^{-1}$
$Re$	Reynolds number
$\dot{s}_k$	rate, $\text{mol m}^{-2} \text{s}^{-1}$
$S$	entropy, $\text{J mol}^{-1} \text{K}^{-1}$
$T$	temperature, K
$u$	velocity, $\text{m s}^{-1}$
$W_k$	molecular weight, $\text{Kg mol}^{-1}$
$[X_k]$	species concentration, $\text{mol m}^{-3}$

$X$  mole fraction

$Y_k$  mass fraction

## Greek letters

$\beta$	symmetry factor
$\delta$	Kronecker delta
$\varepsilon$	emissivity
$\eta_{\text{conc}}$	concentration overpotential, V
$\eta_a, \eta_c$	activation overpotential anode, cathode, V
$\eta_{\text{ohm}}$	ohmic concentration overpotential, V
$\mu$	viscosity, $\text{kg m}^{-1} \text{s}^{-1}$
$\nu$	stoichiometric coefficient reactants
$\nu'$	stoichiometric coefficient products
$\rho$	density, $\text{kg m}^{-3}$
$\sigma$	Stefan Boltzmann constant, $\text{W m}^{-2} \text{K}^{-4}$
$\sigma_e$	conductivity, $\text{S m}^{-1}$
$\phi$	porosity
$\Gamma$	site density, $\text{mol cm}^{-2}$

## Subscript

$a$	anode
$c$	cathode
$e$	electrolyte
$f$	fluid
$g$	gas
$I, ic$	interconnect
$k$	species index

## Abbreviation

DGM dusty gas model

## Acknowledgments

We gratefully acknowledge many fruitful discussions with Professor R.J. Kee and Dr. Huyang Zhu (Colorado School of Mines).

## References

- Ahmed, K., Foger, K., 2000. Kinetics of internal steam reforming of methane on Ni/YSZ based anodes for solid oxide fuel cells. *Catalysis Today* 63, 479–487.
- Bear, J., 1972. *Dynamics of Fluids in Porous Media*. American Elsevier, New York.
- Bieberle, A., 2000. *The electrochemistry of solid oxide fuel cell anodes: experiments, modeling, and simulations*. Ph.D. Thesis.
- Chan, S.H., Xia, Z.T., 2001. Anode micro model of solid oxide fuel cell. *Journal of the Electrochemical Society* 148, A388–A394.

- Chan, S.H., Khor, K.A., Xia, Z.T., 2001. A complete polarization model of a solid oxide fuel cell and its sensitivity to the change of cell component thickness. *Journal of Power Sources* 93, 130–140.
- Chan, S.H., Chen, X.J., Xia, Z.T., 2004. Cathode micro model of solid oxide fuel cell. *Journal of the Electrochemical Society* 151, A164–A172.
- Clarke, S.H., Dicks, A.L., Pinton, K., Smith, T.A., Swann, A., 1997. Intrinsic reaction kinetics of methane steam reforming on a nickel/zirconia anode. *Catalysis Today* 35, 411–423.
- Costmagna, P., Selimovic, A., Borghi, M.D., Agnew, G., 2004. Electrochemical model of the integrated planar solid oxide fuel cell (IP-SOFC). *Chemical Engineering Journal* 102, 61–69.
- Damm, D.L., Federov, A.G., 2005a. Radiation heat transfer in SOFC materials and components. *Journal of Power Sources* 143, 158–165.
- Damm, D.L., Federov, A.G., 2005b. Spectral radiative heat transfer analysis of the planar SOFC. *Journal of Fuel Cell Science and Technology* 2, 258–262.
- Deulhardt, P., Hairer, E., Zugk, J., 1987. One step and extrapolation methods for differential–algebraic systems. *Numerische Mathematik* 51, 501–516.
- Deutschmann, O., Tischer, S., Kleditch, S., Janardhanan, V.M., Correa, C., Chatterjee, D., Warnatz, J., 2004. DETCHEM User Manual Version2.0. ([www.detchem.com](http://www.detchem.com)).
- Dicks, A.L., Pointon, K.D., Siddle, A., 2000. Catalytic aspects of steam reforming of hydrocarbons in internal reforming fuel cells. *Journal of Power Sources* 86, 523–530.
- Finnerty, C.M., Coe, N.J., Cunningham, R.H., Ormerod, R.M., 1998. Carbon formation on and deactivation of Ni-based/zirconia anodes in solid oxide fuel cells running on methane. *Catalysis Today* 46, 137–145.
- Haberman, B.A., Young, J.B., 2004. Three-dimensional simulation of chemically reacting gas flows in the porous support structure of an integrated-planar solid oxide fuel cell. *International Journal of Heat and Mass Transfer* 47, 3617–3629.
- Hall, D.J., 1999. Numerical modeling and performance study of a tubular SOFC. *IEEE Transaction on Energy Conversion* 14, 749–753.
- Hayes, R.E., Kolaczowski, S.T., 1997. *Introduction to Catalytic Combustion*. Gordon and Breach Science Publishers, Amsterdam.
- Hecht, E.S., Gupta, G.K., Zhu, H., Dean, A.M., Kee, R.J., Maier, L., Deutschmann, O., 2005. Methane reforming kinetics within a Ni–YSZ SOFC anode support. *Applied Catalysis A* 295, 40–51.
- Jackson, R., 1977. *Transport in Porous Catalysts*. Elsevier, Amsterdam.
- Janardhanan, V.M., Deutschmann, O., 2006. CFD analysis of a solid oxide fuel cell with internal reforming: coupled interactions of transport, heterogeneous catalysis and electrochemical processes. *Journal of Power Sources* 162, 1192–1202.
- Jiang, Y., Virkar, A.V., 2003. Fuel composition and diluent effect on gas transport and performance of anode supported SOFCs. *Journal of Electrochemical Society* 150, A942–A951.
- Keegan, K., Khaleel, M., Chick, L., Recknagle, K., Simmer, S., Deibler, J., 2002. Analysis of planar solid oxide fuel cell based automotive auxiliary power unit. *SAE Technical Paper Series*, 2002-01-0413.
- Kim, J.W., Vikar, A.V., Fung, K.Z., Mehta, K., Singhal, S.C., 1999. Polarization effects in intermediate temperature anode-supported solid oxide fuel cells. *Journal of the Electrochemical Society* 146, 69–78.
- Larminie, J., Dicks, A., 2003. *Fuel Cell Systems Explained*. second ed. Wiley, New York.
- Lee, S., Vohs, J.M., Gorte, R.J., 2004. A study of SOFC anodes based on Cu–Ni and Cu–Co bimetals in CeO<sub>2</sub>–YSZ. *Journal of the Electrochemical Society* 151, A1319–A1323.
- Li, P.W., Suzuki, K., 2004. *Journal of the Electrochemical Society* 151, A548–A557.
- Li, P.W., Schaefer, L., Chyu, M.K., 2004. A numerical model coupling the heat and gas species transport processes in a tubular SOFC. *Journal of Heat Transfer* 126, 219–229.
- Liu, J., Barnett, S.A., 2003. Operation of anode-supported solid oxide fuel cells in methane and natural gas. *Solid State Ionics* 158, 11–16.
- Mason, E.A., Malinauskas, A.P., 1983. *Gas transport in porous media. The Dusty Gas Model*. Elsevier, Amsterdam.
- Mastusaki, Y., Yasuda, I., 2000. Electrochemical oxidation of H<sub>2</sub> and CO in a H<sub>2</sub>–H<sub>2</sub>O–CO–CO<sub>2</sub> system at the interface of a Ni–YSZ cermet electrode and YSZ electrolyte. *Journal of the Electrochemical Society* 147, 1530–1635.
- McIntosh, S., Vohs, J.M., Gorte, R.J., 2003. Effect of precious-metal dopants on SOFC anodes for direct utilization of hydrocarbons. *Journal of the Electrochemical Society* 6, A240–A243.
- Murray, E.P., Tsai, T., Barnett, S.A., 1999. A direct-methane fuel cell with ceria-based anode. *Nature* 400, 649–651.
- Murthy, S., Federov, A.G., 2003. Radiation heat transfer analysis of the monolith type solid oxide fuel cell. *Journal of Power Sources* 124, 453–458.
- Park, S., Vohs, J.M., Gorte, R.J., 2000. Direct oxidation of hydrocarbons in a solid-oxide fuel cell. *Nature* 404, 265–267.
- Sheng, C.Y., Dean, A.M., 2004. Importance of gas-phase kinetics within anode channel of a solid-oxide fuel cell. *Journal of Physical Chemistry* 108, 3772–3783.
- Steele, B.C.H., 1999. Running on natural gas. *Nature* 400, 619–621.
- Sukeshini, A.M., Habibzadeh, B., Becker, B.P., Stoltz, C.A., Eichhorn, B.W., Jackson, G.S., 2006. Electrochemical oxidation of H<sub>2</sub>, CO, and CO/H<sub>2</sub> mixtures on patterned Ni anodes on YSZ electrolytes. *Journal of the Electrochemical Society* 153, A705–A715.
- Takeguchi, T., Kikuchi, R., Yano, T., Eguchi, K., Murata, K., 2003. Effect of precious metal addition to Ni–YSZ cermet on reforming of CH<sub>4</sub> and electrochemical activity as SOFC anode. *Catalysis Today* 84, 217–222.
- Tanner, C.W., Fung, K.Z., Virkar, A.V., 1997. The effect of porous composite electrode structure on solid oxide fuel cell performance. *Journal of the Electrochemical Society* 144, 21–30.
- VanderSteen, J.D.J., Pharoah, J.G., 2006. Modeling radiation heat transfer with participating media in solid oxide fuel cell. *Journal of Fuel Cell Science and Technology* 3, 62–67.
- Williford, R.E., Chick, L.A., Maupin, G.D., Simmer, S.P., Stevenson, J.W., 2003. Diffusion limitations in the porous anode of SOFCs. *Journal of the Electrochemical Society* 150, A1067–A1072.
- Xu, J., Froment, G.F., 1989. Methane steam reforming, methanation and water–gas shift: I. Intrinsic kinetics. *A.I.Ch.E. Journal* 35, 8–35.
- Zhu, H., Kee, R.J., 2003. A general mathematics model for analyzing the performance of fuel-cell membrane-electrode assemblies. *Journal of Power Sources* 117, 61–74.
- Zhu, J., Ommen, G., Lefferts, L., 2004. Reaction scheme of partial oxidation of methane to synthesis gas over yttrium-stabilized zirconia. *Journal of Catalysis* 225, 388–397.
- Zhu, H., Kee, R.J., Janardhanan, V.M., Deutschmann, O., Goodwin, D., 2005. Modeling elementary heterogeneous chemistry and electrochemistry in solid oxide fuel cells. *Journal of the Electrochemical Society* 152, A2427–A2440.